Nano Research

ISSN 1998-0124 CN 11-5974/O4
https://doi.org/10.26599/NR.2026.94909330

Research Article

Ice-templated lamellar aerogels with magnetic-dielectric synergy derived from Ni-MOF nanoribbons/graphene for ultralight broadband microwave absorption

Xiaogu Huang(✉), Gaoyuan Yu, Jiawen Wei, Gaofeng Shao(✉)
School of Chemistry and Materials Science, Jiangsu Key Laboratory of New Energy Devices and Interface Science, Nanjing University of Information Science & Technology, Nanjing 210044, China

Nano Res., **Just Accepted Manuscript** • https://doi.org/10.26599/NR.2026.94909330
https://www.sciopen.com/journal/1998-0124 on Nov. 13, 2026

© The Authors(s)

Just Accepted

This is a "Just Accepted" manuscript, which has been examined by the peer-review process and has been accepted for publication. A "Just Accepted" manuscript is published online shortly after its acceptance,which is prior to technical editing and formatting and author proofing. Tsinghua University Press (TUP) provides "Just Accepted" as an optional and free service which allows authors to make their results available to the research community as soon as possible after acceptance. After a manuscript has been technically edited and formatted, and the page proofs have been corrected, it will be removed from the "Just Accepted" web site and published officially with volume and article number (e.g., *Nano Research*, **2025**, *18*, 94906990). Please note that technical editing may introduce minor changes to the manuscript text and/or graphics which may affect the content, and all legal disclaimers that apply to the journal pertain. In no event shall TUP be held responsible for errors or consequences arising from the use of any information contained in these "Just Accepted" manuscripts. To cite this anuscript please use its Digital Object Identifier (DOI®),which is identical for all formats of publication.

Just Accepted

Research Article

Ice-templated lamellar aerogels with magnetic-dielectric synergy derived from Ni-MOF nanoribbons/graphene for ultralight broadband microwave absorption

Xiaogu Huang [1] ✉, Gaoyuan Yu [1], Jiawen Wei [1], Gaofeng Shao [1] ✉

[1] School of Chemistry and Materials Science, Jiangsu Key Laboratory of New Energy Devices and Interface Science, Nanjing University of Information Science & Technology, Nanjing 210044, China

Received: 24 July 2026; **Revised: 22 October 2026**; **Accepted: 13 November 2026**

✉ Address correspondence to Xiaogu Huang, hxg@nuist.edu.cn; Gaofeng Shao, gfshao@nuist.edu.cn

Cite this article: *Nano Research*, 2027, 20, 94909330 https://doi.org/10.26599/NR.2026.94909330

ABSTRACT: Lightweight microwave absorbers that simultaneously achieve strong attenuation and broad effective absorption bandwidths are highly desirable for electromagnetic protection and stealth applications. Herein, ultralight lamellar magnetic–dielectric aerogels are fabricated by coupling Ni–MOF nanoribbons with graphene oxide via an ice–templating assembly process, followed by carbonization. Strong interfacial compatibility between the Ni–MOF nanoribbons and graphene oxide facilitates their integration into hybrid building blocks, which are subsequently structured into aligned porous channels during ice-templating. Following carbonization, the magnetic components derived from the Ni–MOF nanoribbons become intimately coupled with graphene–derived carbon sheets, creating abundant magnetic–dielectric heterointerfaces throughout the lamellar porous framework. This hierarchical configuration enables tailorable electromagnetic parameters, thereby balancing impedance matching and attenuation capability. By systematically adjusting the carbonization temperature and the initial mass ratio of Ni–MOF nanoribbons to graphene oxide, the electromagnetic response of the aerogels was optimized. Notably, the optimized aerogel features an ultralow density of 4.45 mg·cm^{-3}, while achieving a minimum reflection loss of −64 dB at 16.72 GHz with a matching thickness of 2.8 mm, alongside a maximum effective absorption bandwidth of 9.0 GHz at 3.4 mm. Furthermore, radar cross–section simulations indicate the potential of the aerogel for suppressing electromagnetic scattering under simulated far-field conditions. This work provides an effective strategy for constructing ultralight lamellar magnetic–dielectric aerogels for broadband microwave absorption.

KEYWORDS: Metal–organic frameworks, graphene aerogels, magnetic–dielectric heterointerfaces, anisotropic porous structure, broadband microwave absorption

Just Accepted

1 Introduction

The rapid advancement of electronic communication technologies and radar systems has exacerbated electromagnetic interference and radar detection risks [1-7]. Consequently, there is a distinct demand for lightweight microwave absorbers that can simultaneously exhibit strong attenuation capability and broad effective absorption bandwidth (EAB) for electromagnetic protection and stealth applications [8-11].

To date, considerable efforts have been devoted to the design of high−performance microwave absorbers, spanning magnetic materials [12-14], carbon–based materials [15-20], conductive polymers [21, 22], ceramics [23-26], and their hybrid composites [27-29]. Although many conventional microwave absorbers achieve strong attenuation at specific frequencies, their narrow EAB struggles to satisfy the growing need for broadband protection. Recently, carbon aerogels have emerged as highly promising lightweight candidates because of their three – dimensional porous architectures and low−density characteristics [30, 31]. These interconnected porous networks can not only minimize the overall density but also promote multiple reflection and scattering of incident electromagnetic waves, thereby improving impedance matching via abundant air – solid interfaces. Among various precursors for carbon aerogels, graphene oxide (GO) is particularly attractive because its two – dimensional sheet – like morphology, abundant oxygen−containing functional groups, and excellent aqueous dispersibility are favorable for constructing graphene−based aerogel frameworks [16]. Following thermal treatment, GO – derived graphene networks form electrical conduction pathways and defect – rich polarization sites that facilitate electromagnetic energy dissipation. However, pristine graphene aerogels rely predominantly on dielectric loss mechanisms, such as conduction loss and dipolar polarization, inherently restricting their attenuation pathways [32]. Moreover, excessive conductivity in pure graphene often induces impedance mismatch, impeding the simultaneous realization of strong attenuation and broad EABs [33]. Therefore, rationally integrating magnetic components into graphene−based aerogels is considered an effective strategy to enrich attenuation mechanisms, balance impedance matching, and boost broadband microwave absorption performance [34].

Metal – organic frameworks (MOFs), a class of crystalline porous materials with tailorable compositions and well−defined structures, have garnered immense interest as

precursors for electromagnetic functional materials [35-37]. During thermal treatment, MOFs convert into metallic, metal–oxide, or carbon–containing derivatives while largely preserving their original structural topologies [38, 39]. In particular, Ni – based MOFs are promising precursors because their Ni – containing derivatives can introduce magnetic responses and magnetic–dielectric coupling effects, thereby benefiting microwave attenuation. Beyond mere compositional design, the specific morphology of the MOF precursors dictates the ultimate microstructure, interfacial configuration, and electromagnetic response of the derived absorbers. Compared with conventional particulate MOF, ribbon – like Ni – MOF nanoribbons offer unique anisotropic structural features, expanded contact areas with GO nanosheets, and highly continuous magnetic – dielectric interfacial networks after carbonization [40]. Therefore, integrating Ni–MOF nanoribbons with a GO matrix presents a compelling approach for constructing lightweight magnetic – dielectric graphene aerogels with tailorable electromagnetic parameters and broadband microwave absorption capability.

Herein, ultralight anisotropic magnetic – dielectric graphene aerogels derived from Ni – MOF nanoribbons and GO were fabricated through ice–templating assembly, freeze–drying, and carbonization. During carbonization, GO evolved into conductive graphene cell walls, while Ni – MOF nanoribbons were converted into Ni – containing magnetic nanodomains, yielding an integrated magnetic – dielectric porous architecture. The structural evolution, electromagnetic parameters, and microwave absorption performance were systematically tuned by adjusting the carbonization temperature and the precursor mass ratios. The optimized aerogel exhibits a minimum reflection loss of – 64 dB at 16.72 GHz under a matching thickness of 2.8 mm and a maximum EAB of 9.0 GHz at 3.4 mm. Ultimately, this work outlines a rational methodology for generating lightweight, MOF – derived magnetic – dielectric graphene aerogels, offering valuable insights into the design of high-performance broadband microwave absorbers grounded in anisotropic porous frameworks.

2 Experimental

2.1. Synthesis of Ni–MOF Nanoribbons

Ni – MOF nanoribbons were synthesized via a solvothermal method. In a typical procedure, 300 mg of $Ni(CH_3COO)_2{\cdot}4H_2O$ was dispersed in 90 mL of absolute ethanol under magnetic stirring. Subsequently, 300 mg of $C_5H_4O_2S$ was added to the above solution, followed by stirring for 1 h. The resulting mixture was then transferred to a Teflon – lined autoclave and heated at 150 °C for 12 h. After naturally cooling to room temperature, the obtained Ni – MOF nanoribbons were collected by centrifugation and washed with absolute ethanol and deionized water three times. Finally, the products were dried under vacuum at 60 °C for 12 h to obtain Ni–MOF nanoribbons.

2.2. Preparation of Ni–MOF/GO–Derived Aerogels

Ni – MOF nanoribbons/GO aerogels were prepared through an ice – templating assembly strategy [41]. For the representative sample with a Ni–MOF/GO mass ratio of 1:1, Ni – MOF nanoribbons were first dispersed in 2 mL of deionized water, followed by the addition of 4 mL of GO aqueous dispersion with a concentration of 10 mg mL^{-1}. The mixture was then ultrasonicated to form a homogeneous dispersion. Separately, sodium alginate (SA) aqueous solution with a concentration of 20 mg mL^{-1} was prepared by dissolving 2 g of SA in 100 mL of deionized water under stirring at 60 °C. Subsequently, the SA solution was added to the Ni–MOF/GO dispersion according to a GO/SA mass ratio of 3:1, followed by stirring for 20 min. During directional freezing of the above dispersion, the unidirectional growth of ice crystals induced the formation of an ordered Ni – MOF/GO gel. Specifically, the bottom of the mold was exposed to the liquid-nitrogen cold source, generating a unidirectional temperature gradient along the vertical direction. Consequently, ice crystals grew predominantly from the bottom to the top of the mold, inducing the formation of aligned lamellar channels. SA was introduced mainly as a water-soluble binder and structural stabilizer to maintain the homogeneity of the Ni–MOF/GO dispersion and improve the integrity of the assembled framework during directional freezing and freeze – drying, thereby helping stabilize the resulting lamellar architecture. The obtained gel was further frozen for 24 h and then freeze–dried for 24 h to obtain the Ni–MOF/GO aerogel.

The Ni – MOF/GO – derived aerogels were obtained by thermal treatment of the as–prepared Ni–MOF/GO aerogels. Specifically, the aerogels were heated to 500, 600, or 700 °C under a N_2 atmosphere at a heating rate of 3 °C min^{-1} and maintained for 1 h. After the thermal treatment, ultralight Ni – MOF/GO – derived magnetic – dielectric aerogels were obtained. Samples with different Ni – MOF/GO mass ratios were prepared using the same procedure by adjusting the feeding ratio of Ni – MOF nanoribbons to GO. For clarity, the obtained samples were denoted as NiCG–x. NiCG–1, NiCG–2, and NiCG–3 correspond to the samples prepared with a Ni-MOF/GO mass ratio of 2:1 and carbonized at 500, 600, and 700 °C, respectively. NiCG–4 and NiCG–5 were prepared at 700 °C with Ni-MOF/GO mass ratios of 1:1 and 1:2, respectively.

2.3. Characterization

The morphology and microstructure of the Ni – MOF nanoribbons and Ni – MOF/GO – derived aerogels were characterized by field – emission scanning electron microscopy (FESEM, Zeiss Ultra–55). Transmission electron microscopy (TEM, FEI Tecnai G2 20 TWIN) was employed to further observe the internal structure and nanoscale components of the samples. Elemental distributions were analyzed by EDS mapping using an energy–dispersive X–ray spectrometer attached to the electron microscope. The crystalline phases were identified by powder X – ray diffraction (XRD, Rigaku, Cu Kα radiation, 40 kV, 40 mA, D/teX Ultra 250 detector) over a scanning range of 10–80°. X – ray photoelectron spectroscopy (XPS, Thermo Scientific K–Alpha) was performed to investigate the surface chemical states and elemental compositions. Raman spectroscopy (Renishaw InVia) was used to evaluate the carbon structure and graphitization degree of the aerogels. The magnetic properties were measured using a vibrating sample magnetometer (VSM, Lakeshore).

The complex permittivity and permeability were measured by the coaxial–line method using a vector network analyzer. For electromagnetic parameter measurements, the monolithic Ni – MOF/GO derived aerogels were directly infiltrated with molten paraffin wax without pulverization. The paraffin-infiltrated aerogels were then cut into standard

Just Accepted

toroidal specimens with an outer diameter of 7.00 mm and an inner diameter of 3.04 mm. The filling fraction of the aerogel in the paraffin matrix was calculated according to the following equation:

$$w = \rho_{aerogel} \times v_{ring}/m_{ring} \quad (1)$$

where $\rho_{aerogel}$ represents the density of the aerogel, and V_{ring} and m_{ring} are the volume and mass of the toroidal specimen, respectively.

2.4. RCS Simulation

The radar cross–section (RCS) performance of the Ni–MOF/GO derived aerogel was evaluated using CST Studio Suite 2019. A perfect electric conductor (PEC) plate with dimensions of 200 mm × 200 mm × 1 mm was used as the substrate, and the aerogel absorber was placed on the PEC plate to construct the microwave absorption model. According to the optimized microwave absorption performance, the absorber thickness was set to 2.8 mm for the NiCG–3 aerogel at 16.72 GHz. Open boundary conditions were applied along the x, y, and z directions. Linearly polarized electromagnetic waves were incident from the positive Y–axis, with the electric field polarization direction along the Z–axis.

3 Results and discussion

As schematically shown in Fig. 1a, ultralight lamellar magnetic – dielectric aerogels were fabricated by ice-templating, freeze–drying, and subsequent carbonization. A homogeneous suspension containing Ni–MOF nanoribbons, GO, and SA was first subjected to unidirectional freezing with liquid nitrogen as the cold source. During unidirectional freezing, the anisotropic growth of ice crystals directed the co–assembly of Ni–MOF nanoribbons and GO sheets along the temperature gradient, thereby generating an ordered lamellar ice–templated framework. After freeze–drying and subsequent carbonization, the directional architecture was largely retained, yielding a lightweight aerogel with an interconnected anisotropic porous network [42]. As shown in Fig. S1, the monolithic aerogel can be readily supported by lightweight objects and rapidly attracted by a magnet, visually demonstrating its ultralight nature and magnetic responsiveness. The phase evolution of the aerogels was investigated by XRD analysis. As shown in Fig. 1b, all samples exhibit a broad diffraction feature at 20–30°, which can be assigned to amorphous and graphene–derived carbon structures. After carbonization, three distinct diffraction peaks appear at approximately 44.5°, 51.8°, and 76.4°, corresponding to the (111), (200), and (220) planes of metallic Ni, respectively [43]. In addition, the diffraction signals associated with Ni_3S_2 indicate that the Ni – MOF precursor was successfully converted into Ni – and Ni_3S_2–containing derivatives during thermal treatment [44]. When comparing NiCG–1, NiCG–2, and NiCG–3, the Ni– and Ni_3S_2–related diffraction features become more pronounced with increasing carbonization temperature, indicating enhanced crystallinity and more complete thermal

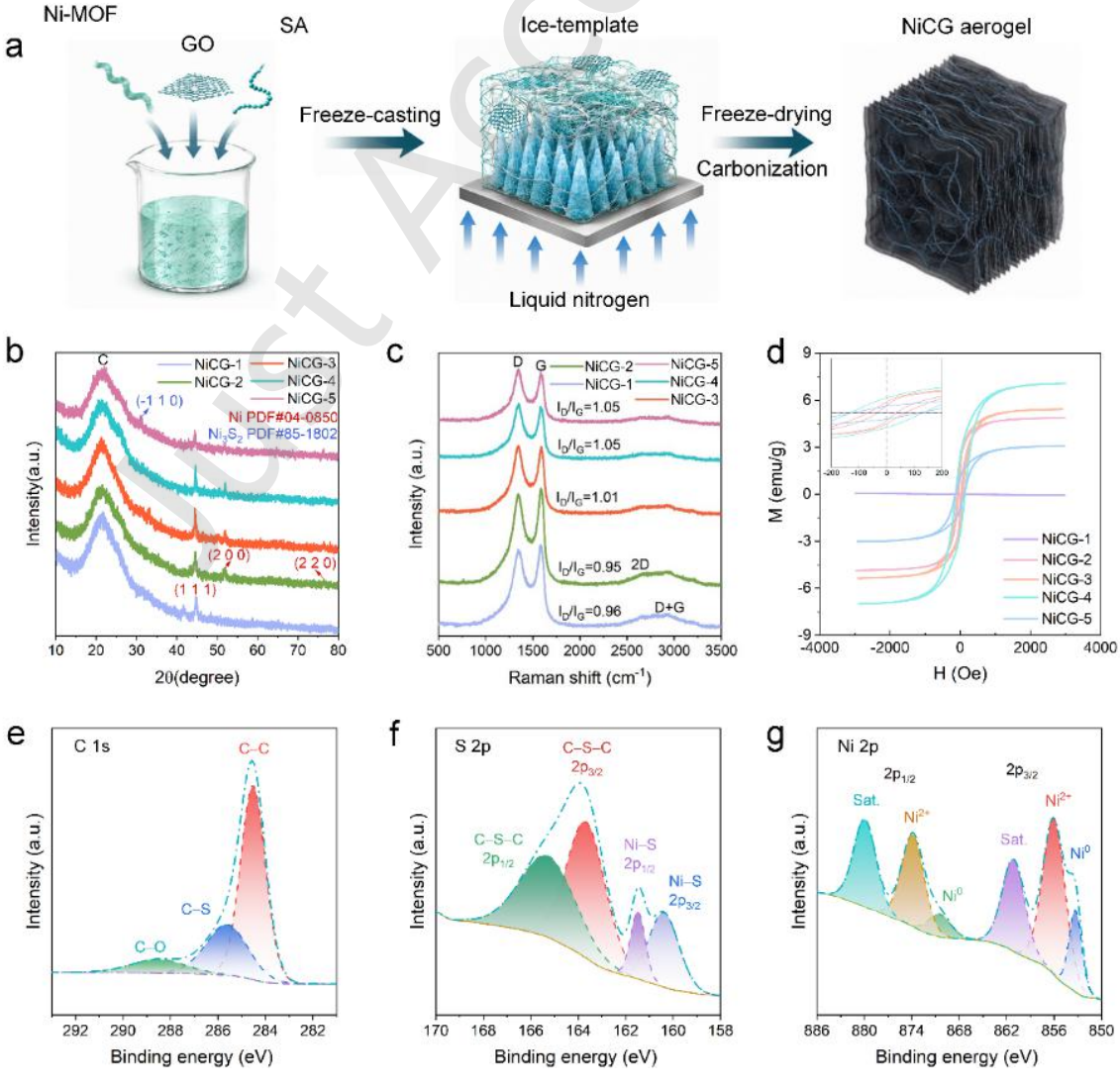

Figure 1 (a) Schematic illustration of the fabrication process of NiCG aerogels. (b) XRD patterns, (c) Raman spectra, (d) magnetic hysteresis loops, and (e–g) high–resolution XPS spectra of (e) C 1s, (f) S 2p, and (g) Ni 2p for the NiCG–3 aerogel.

Just Accepted

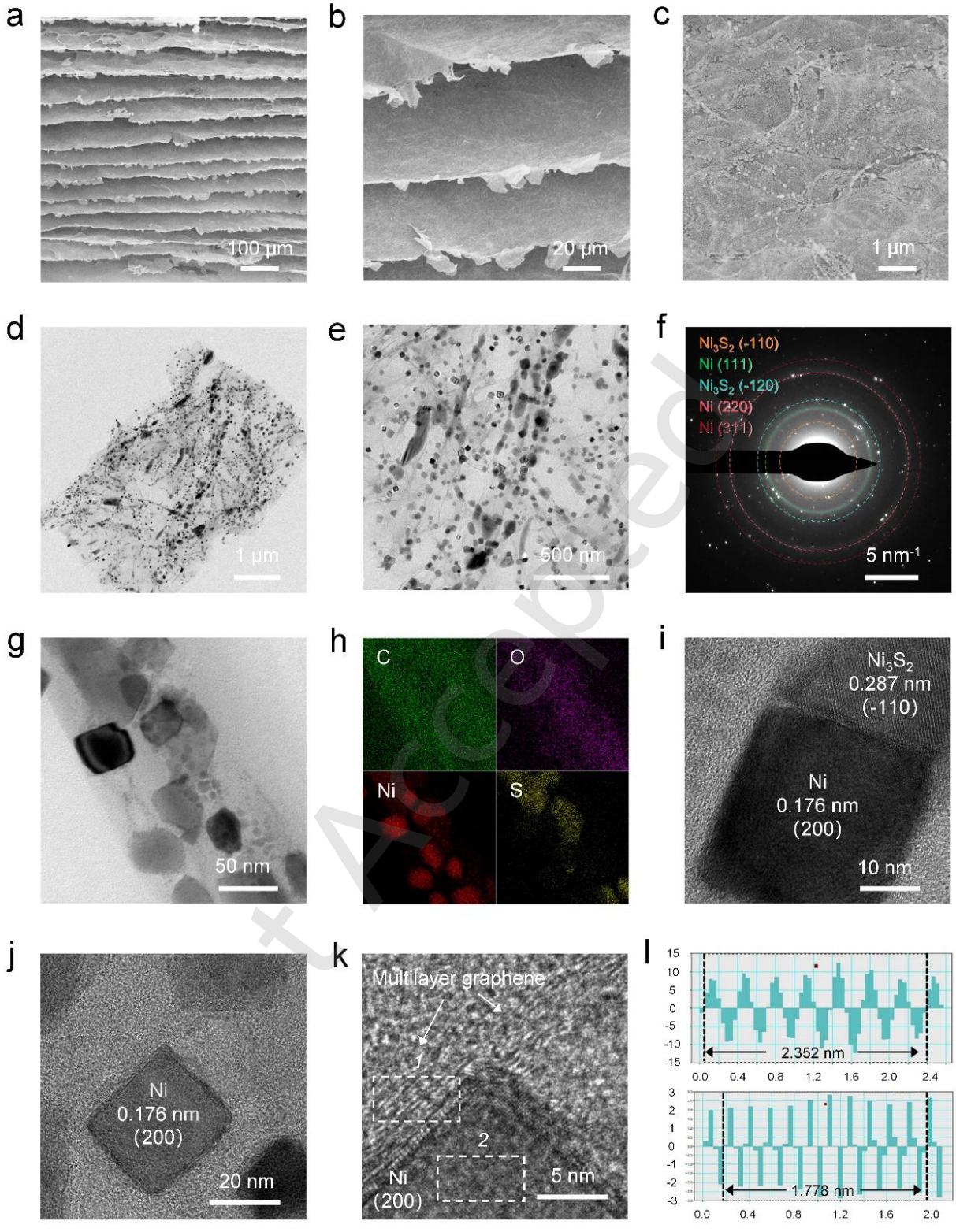

Figure 2 (a–c) SEM images, (d, e, g) TEM images, (f) SAED pattern, (h) EDS elemental mapping images, (i–k) HRTEM images, and (l) line profiles corresponding to the selected regions in (k) of the NiCG–3 aerogel.

conversion of the Ni–MOF-derived components. In contrast, comparison among NiCG–3, NiCG–4, and NiCG–5 shows that variation in the Ni–MOF/GO ratio mainly changes the relative diffraction contribution of the Ni-containing crystalline phases and the graphene-derived carbon component. With increasing GO proportion, the relative contribution of the Ni–MOF–derived phases decreases, while no additional crystalline phase is observed. Raman spectroscopy was further employed to evaluate the structural characteristics of the carbon framework in the aerogels. As shown in Fig. 1c, all samples show two characteristic peaks at approximately 1340 and 1580 cm^{-1}, corresponding to the D and G bands of carbon materials, respectively. The D band is associated with disordered carbon and structural defects, whereas the G band originates from graphitic carbon domains. The intensity ratio of the D band to the G band (I_D/I_G) is generally used to assess the defect density and graphitization degree of carbon

Accepted

structures [45]. The comparable intensities of the D and G bands indicate the formation of a defective but partially graphitized carbon framework, in which graphitic domains can facilitate electron transport, whereas abundant defect sites can serve as polarization centers for dielectric relaxation. The weak 2D band in the high – wavenumber region further suggests the formation of graphene – derived carbon domains after thermal treatment [46]. The magnetic properties of the aerogels were evaluated using magnetic hysteresis loop measurements. As shown in Fig. 1d, the carbonized samples exhibit obvious magnetic responses, which originate from the formation of MOF – derived Ni – containing magnetic components. The saturation magnetization varies with both the carbonization temperature and the initial mass ratio of Ni – MOF to GO, indicating that the content of magnetic components and the overall magnetic response can be effectively regulated through precursor composition and thermal treatment. Such tunable magnetism provides a basis for magnetic loss and magnetic–dielectric coupling effects during microwave attenuation [37]. As shown in Fig. 1e–g, XPS was further employed to examine the surface chemical states and bonding configurations of the carbonized aerogels. The high – resolution C 1s spectrum of NiCG – 3 can be deconvoluted into C – C/C=C, C – S related, and C – O related components, indicating the formation of graphene-derived carbon structures with residual oxygen – and sulfur–containing functionalities [44]. In the S 2p region, the fitted peaks centered at approximately 160.4 and 161.5 eV can be assigned to Ni – S $2p_{3/2}$ and Ni – S $2p_{1/2}$, respectively, while the peaks located at approximately 163.8 and 165.4 eV correspond to C – S – C $2p_{3/2}$ and C – S – C $2p_{1/2}$, respectively. This suggests that sulfur exists in both nickel-sulfide and carbon-bonded chemical environments after carbonization. The Ni 2p spectrum shows the coexistence of metallic Ni^0 and Ni^{2+} species, accompanied by satellite peaks, revealing mixed Ni chemical environments [47]. The O 1s spectrum further confirms the presence of residual oxygen-containing species (Fig. S2), while the absence of a distinct lattice Ni–O component suggests that surface oxidation/hydroxylation may only partially contribute to the Ni^{2+} signal.

The microstructure and hierarchical anisotropic architecture of the optimized NiCG – 3 magnetic – dielectric aerogel were systematically characterized by SEM. After carbonization, the aerogel largely retained the ice – templated lamellar configuration, with parallel channels clearly observed over a large area (Fig. 2a), confirming the directional assembly of Ni–MOF nanoribbons and GO sheets induced by anisotropic ice – crystal growth during unidirectional freezing. A magnified SEM image shows that adjacent lamellae are separated by open interlayer spaces and interconnected by continuous sheet–like walls (Fig. 2b), forming an anisotropic porous network that can provide extended transport channels for incident microwaves and promote multiple internal reflections [48]. At higher magnification, abundant nanoparticles are observed on the surface of the graphene – derived lamellae (Fig. 2c), suggesting that the Ni – MOF nanoribbons underwent confined in situ transformation during carbonization, generating Ni – based derivatives anchored on the graphene – derived carbon skeleton. With increasing GO content, sheet overlap and restacking become more pronounced, particularly for NiCG – 5, resulting in a relatively denser porous framework with reduced interlayer openness (Fig. S3 and S4).

To gain deeper insight into the nanoscale structural characteristics of NiCG, TEM was employed to investigate the distribution and interfacial configuration of the derived components (Fig. S5). For the optimized NiCG – 3, abundant nanoparticles and residual nanoribbon – like fragments are anchored on wrinkled graphene–derived carbon sheets (Fig. 2d, e). Such a structure enables intimate interfacial coupling between MOF – derived Ni – containing magnetic nanodomains and graphene – derived dielectric carbon sheets, thereby favoring the construction of magnetic–dielectric heterointerfaces [49]. The selected–area electron diffraction pattern (Fig. 2f) displays several distinct diffraction rings, which can be indexed to metallic Ni and Ni_3S_2 phases. The enlarged TEM image shows that the nanoparticles are tightly attached to the thin carbon sheets (Fig. 2g), indicating intimate interfacial contact rather than simple physical mixing. Elemental mapping (Fig. 2h) reveals the spatial distribution of C, O, Ni, and S, with Ni and S signals mainly concentrated in the particle regions, consistent with the formation of Ni – and Ni_3S_2 – related components and their localized integration with the carbon framework.

HRTEM was further employed to resolve the local crystalline features. As shown in Fig. 2i, lattice spacings of 0.287 and 0.176 nm correspond to the (–110) plane of Ni_3S_2 and the (200) plane of metallic Ni, respectively. A similar lattice spacing of 0.176 nm assigned to metallic Ni is also observed in Fig. 2j, further confirming the formation of Ni nanocrystals during carbonization [50]. Notably, multilayer graphene domains can be identified near the Ni nanocrystals (Fig. 2k), and the corresponding line profiles (Fig. 2l) further verify the locally ordered carbon lattice contrast. These observations confirm the coexistence of Ni – containing magnetic nanodomains, partially graphitized carbon regions, and abundant magnetic – dielectric heterointerfaces within the NiCG–3 framework.

To elucidate the influence of carbonization temperature and rGO content on the dielectric response of NiCG aerogels, their complex permittivity and dielectric attenuation characteristics were systematically analyzed [51]. The real part of permittivity (ε') reflects the electric – field energy storage capability of a material, whereas the imaginary part (ε'') represents its dielectric dissipation capability under an alternating electromagnetic field. As shown in Fig. 3a, all NiCG samples exhibit typical frequency–dispersion behavior, with both ε' and ε'' decreasing gradually with increasing frequency. This frequency – dependent decrease can be attributed to the delayed response of charge carriers and polarization dipoles at high frequencies, where rapid field reversal limits complete charge migration and dipole reorientation [52]. As the carbonization temperature increases from 500 to 700 °C, the ε' and ε'' values of NiCG–1, NiCG – 2, and NiCG – 3 progressively increase. This indicates that higher carbonization temperature promotes the thermal evolution of GO and Ni–MOF nanoribbons, leading to a more developed graphene – derived carbon framework and more effective charge – transport pathways. As a result, electron migration and microcurrent – induced dielectric dissipation are strengthened. Meanwhile, thermally induced structural reconstruction can generate abundant defects, residual functional groups, and heterogeneous interfaces, which serve as polarization centers and further contribute to dielectric relaxation loss [16]. With increasing rGO content from NiCG–3 to NiCG–5, ε' and ε'' further increase, which can

Under Review

be attributed to the formation of a more developed graphene–derived conductive network.

polarization – related loss plays an important role in the dielectric attenuation of NiCG aerogels. This behavior arises

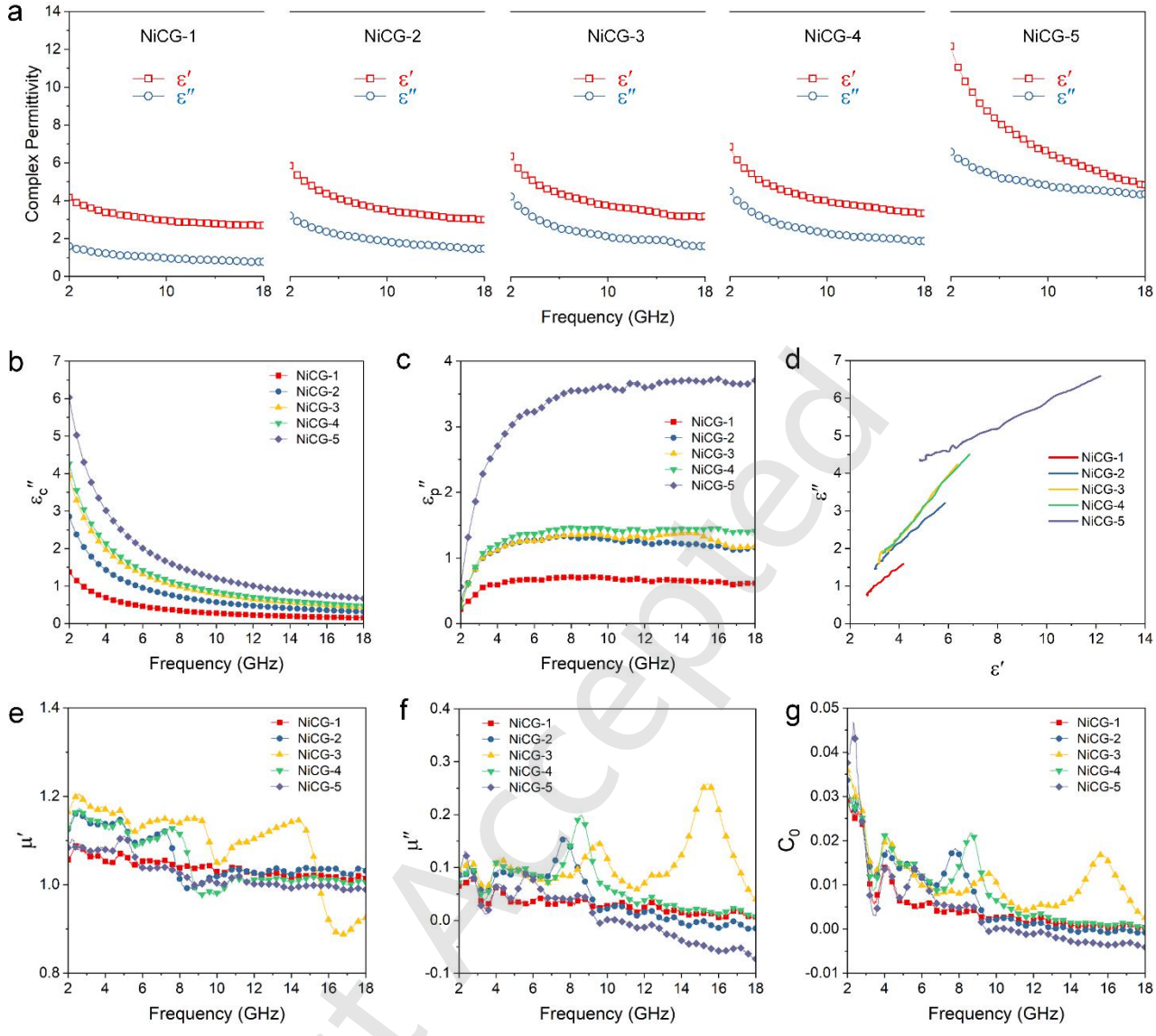

Figure 3 (a) Complex permittivity, (b) ε_c'', (c) ε_p'', (d) Cole–Cole curves, (e) μ', (f) μ'', and (g) C_0 values of the NiCG aerogels at 2–18 GHz.

However, the enhanced complex permitti vity should not be simply regarded as beneficial for microwave absorption, because excessive conductivity and overly high permittivity may deteriorate impedance matching and hinder the effective penetration of incident microwaves into the absorber. To further clarify the origin of dielectric attenuation, ε″ was divided into the conduction loss component (ε_c''), associated with charge transport, and the polarization relaxation component (ε_p''), arising from polarization relaxation processes [53, 54]. The corresponding calculation equations are provided in the Supporting Information [55]. As shown in Fig. 3b, ε_c'' decreases rapidly in the low–frequency region and then gradually levels off at higher frequencies, indicating that conduction loss contributes more prominently at low frequencies. This behavior is closely related to the frequency – dependent migration ability of charge carriers within the graphene – derived carbon network. In contrast, ε_p'' exhibits distinct frequency–dependent behavior (Fig. 3c). The contribution of polarization relaxation becomes more pronounced in the high – frequency region, indicating that from the coexistence of multiple polarization processes. Structural defects and residual functional groups can act as dipolar polarization centers, whereas multiphase heterogeneous interfaces promote interfacial polarization through charge accumulation under an alternating electromagnetic field. These contributions collectively account for the polarization–related dielectric loss. Notably, NiCG–5 exhibits the highest ε_p'' value, which may be related to the enlarged interfacial contact between graphene and Ni – MOF derived components, as well as the increased density of defective carbon regions. These features increase the density of polarization centers and promote interfacial charge accumulation under alternating electromagnetic fields [56]. The dielectric relaxation behavior of the NiCG aerogels was further examined using Cole – Cole plots (Fig. 3d). Unlike an ideal single-Debye relaxation process, which typically produces a well – defined semicircle, the NiCG samples exhibit elongated and non – ideal Cole – Cole trajectories [57]. This deviation from ideal semicircular behavior indicates that the dielectric response cannot be described by a single Debye relaxation process. Combined

Just Accepted

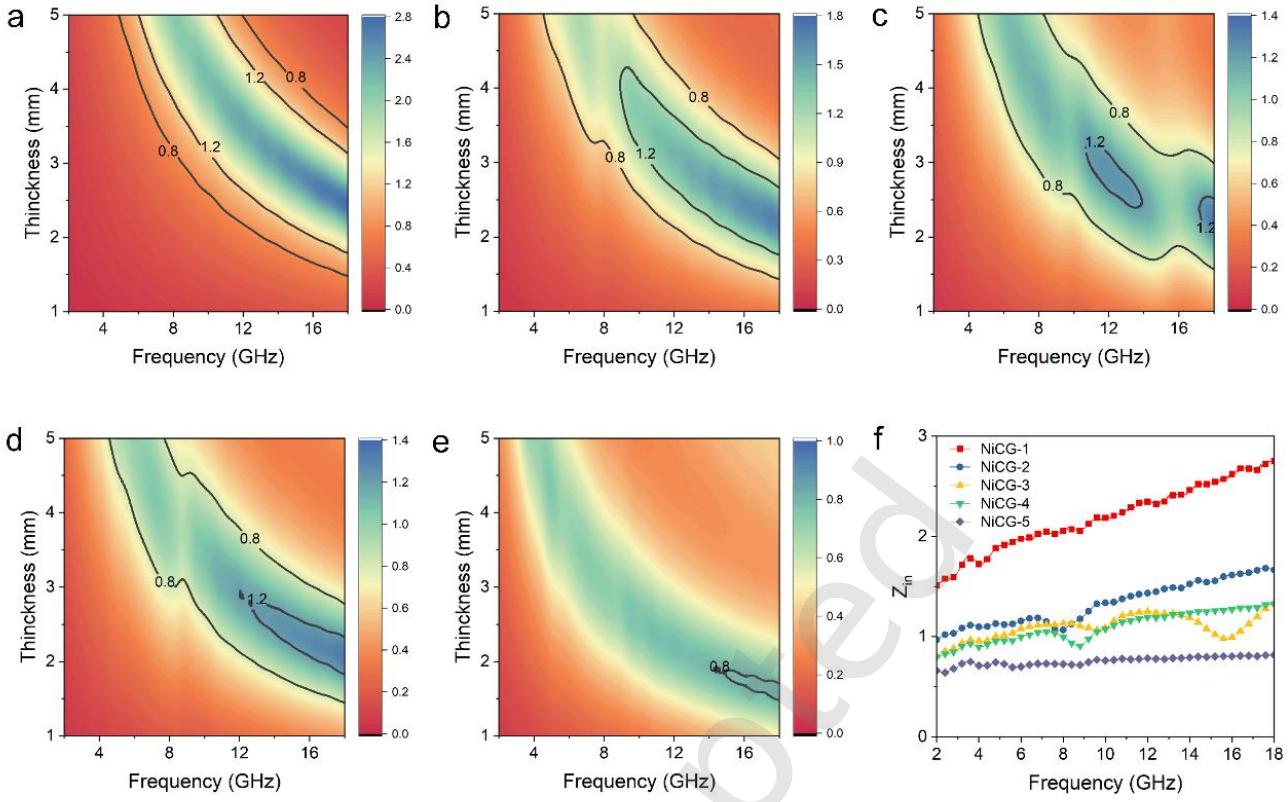

Figure 4 (a–e) 2D impedance matching maps and (f) Z_{in}–f curves of the NiCG aerogels.

with the ε_c'' and ε_p'' analyses, the dielectric attenuation of the NiCG aerogels is attributed to the coexistence of conduction loss and multiple polarization relaxation processes, including defect–induced dipolar polarization and interfacial polarization at heterogeneous interfaces [58]. The magnetic response behavior of the NiCG aerogels was analyzed based on their complex permeability, as shown in Fig. 3e, f. In the frequency range of 2 – 18 GHz, the μ′ values of all NiCG samples fluctuate mainly between 1.0 and 1.2, accompanied by evident frequency – dispersion behavior [59, 60]. The relatively low μ′ values can be attributed to the limited content of Ni – containing magnetic components in the aerogel–paraffin composite system, whereas the fluctuations in μ′ indicate frequency – dependent magnetic relaxation behavior in the samples. With increasing carbonization temperature, the μ′ values of NiCG–1, NiCG–2, and NiCG–3 gradually increase, suggesting that a higher carbonization temperature promotes the thermal transformation of Ni–MOF nanoribbons into Ni–containing magnetic species, thereby improving the magnetic response of the aerogel framework. However, when the rGO content is further increased from NiCG–3 to NiCG–5, the μ′ values no longer increase monotonically. This result indicates that excessive rGO mainly enhances the dielectric and conductive responses rather than the magnetic response and may also reduce the relative contribution of Ni–containing magnetic species within the composite system.

Compared with μ′, μ″ more directly reflects the magnetic dissipation capability [61, 62]. NiCG – 1 exhibits weak μ″ values over the entire frequency range, indicating insufficient magnetic dissipation capability due to the limited formation of Ni–containing magnetic domains at lower carbonization temperature. In contrast, distinct μ″ relaxation peaks are observed for NiCG – 2, NiCG – 3, and NiCG–4, suggesting the involvement of magnetic relaxation and resonance processes during microwave attenuation. Notably, NiCG – 3 shows a pronounced μ″ peak in the high–frequency region, whereas NiCG–4 exhibits a relatively strong μ″ peak in the mid – frequency region. The slightly negative μ″ values of NiCG – 5 at high frequencies can be associated with electromagnetic coupling in the conductive magnetic/carbon system, where the induced magnetic field partially counteracts the external magnetic field [63, 64]. The differences in the position and intensity of these resonance features can be related to the structural evolution of the Ni – containing magnetic components. Increasing the carbonization temperature promotes the formation and crystallization of Ni – and Ni_3S_2 – containing nanodomains, thereby altering their magnetic anisotropy and magnetic interactions. Meanwhile, variation in the Ni–MOF/GO ratio changes the relative content and local environment of these magnetic nanodomains within the graphene-derived carbon framework, which further affects their resonance behavior [34].

The magnetic loss mechanism was further analyzed using the eddy – current loss coefficient C_0, as shown in Fig. 3g. According to the eddy–current loss criterion, if magnetic loss is dominated by eddy – current loss, the C_0 values should remain nearly constant with increasing frequency [65]. In contrast, the C_0 curves of the NiCG samples exhibit evident frequency dependence, including a rapid decrease in the low – frequency region and several relaxation peaks in the mid– and high–frequency regions. This result indicates that the magnetic loss of NiCG aerogels is not solely governed by eddy–current loss but also involves magnetic relaxation and resonance–related dissipation mechanisms. For NiCG–3, the C_0 peak in the high – frequency region corresponds well to the μ″ relaxation peak, further confirming the contribution of magnetic resonance–related dissipation to magnetic loss.

The impedance matching characteristics of the NiCG

Just Accepted

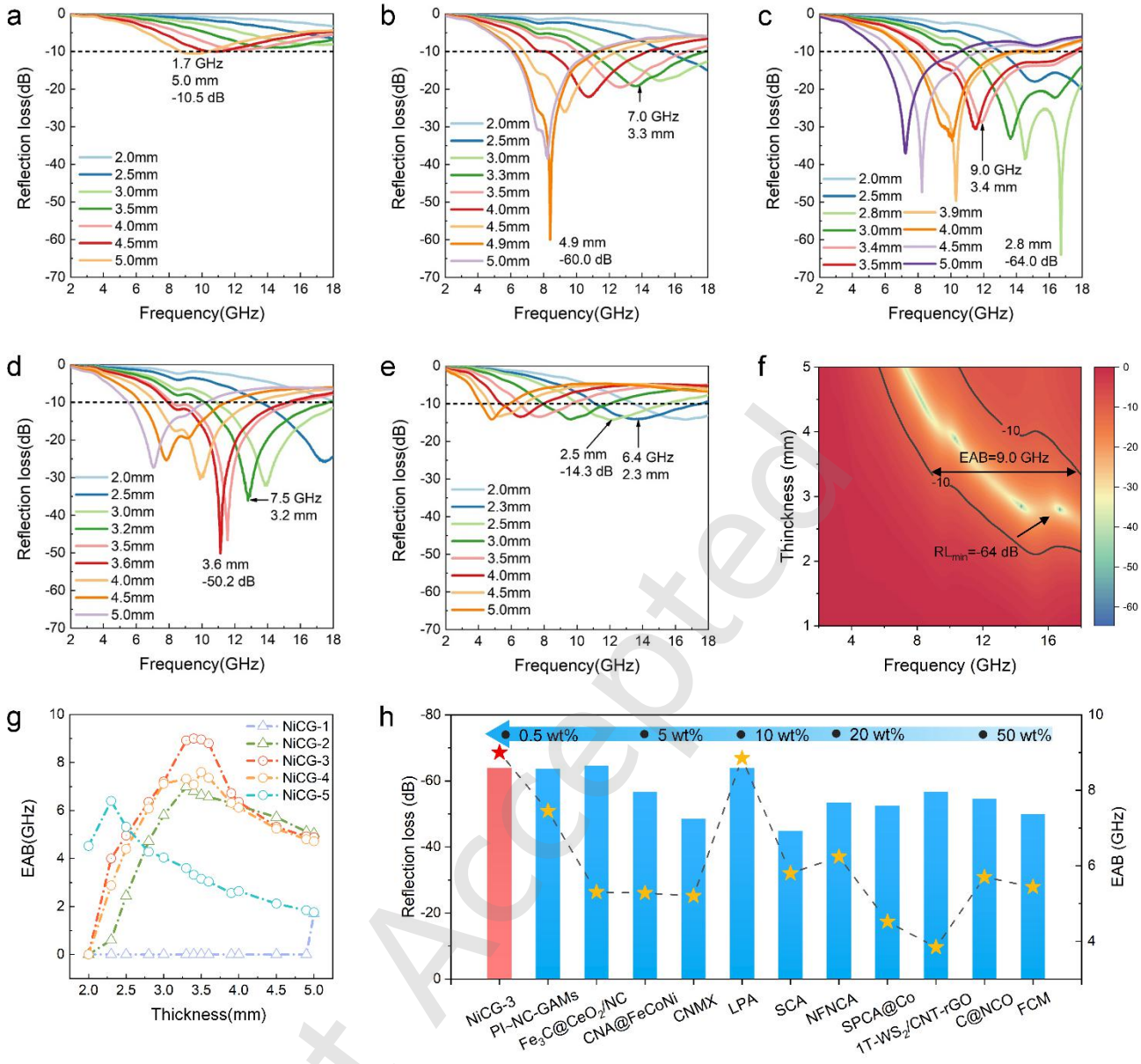

Figure 5 RL–f curves of (a) NiCG–1, (b) NiCG–2, (c) NiCG–3, (d) NiCG–4, and (e) NiCG–5. (f) 2D RL plots of NiCG–3. (g) EAB as a function of thickness for the NiCG aerogels. (h) Comprehensive comparison of the electromagnetic wave absorbing performance in terms of RL_{min}, EAB, and filler content with reported aerogel–based electromagnetic wave absorbing materials, which are listed in Table S1 in the Supporting Information.

aerogels were evaluated using the normalized input impedance $|Z_{in}/Z_0|$, as shown in Fig. 4a–f. In general, efficient microwave absorption requires incident electromagnetic waves to effectively enter the absorber before being dissipated through dielectric and magnetic losses [66-68]. Therefore, a normalized input impedance close to unity is essential for minimizing surface reflection and enabling electromagnetic wave penetration. The two – dimensional impedance maps reveal that NiCG – 1 exhibits a narrow impedance–matched region, mainly distributed at relatively large thicknesses and high frequencies. Meanwhile, its frequency – dependent impedance value is significantly higher than unity, suggesting a pronounced deviation from the optimal matching condition. With increasing carbonization temperature, the impedance–matched regions of NiCG – 2 and NiCG – 3 gradually expand, indicating improved coordination between complex permittivity and complex permeability. In particular, NiCG–3 shows a broad impedance – matched region within the $|Z_{in}/Z_0|$ = 0.8 – 1.2 contour range, covering a relatively wide frequency – thickness domain. This improvement can be attributed to the optimized balance between Ni–containing magnetic components and the rGO – derived conductive framework, which regulates the dielectric – magnetic response and reduces impedance mismatch. Further increasing the rGO content substantially alters the impedance matching behavior. Although NiCG – 4 still maintains a relatively effective impedance–matched region, its matching distribution is less favorable than that of NiCG – 3. For NiCG – 5, the normalized impedance remains below unity over most of the measured frequency range, and the impedance–matched region is markedly narrowed. This phenomenon is closely associated with the overdeveloped conductive network caused by excessive rGO content. Excessive rGO breaks the balance between complex permittivity and complex permeability, thereby deteriorating impedance matching.

The microwave absorption performance of the NiCG aerogels was evaluated using reflection loss (RL) curves at different sample thicknesses [69]. Generally, an RL value

Just Accepted

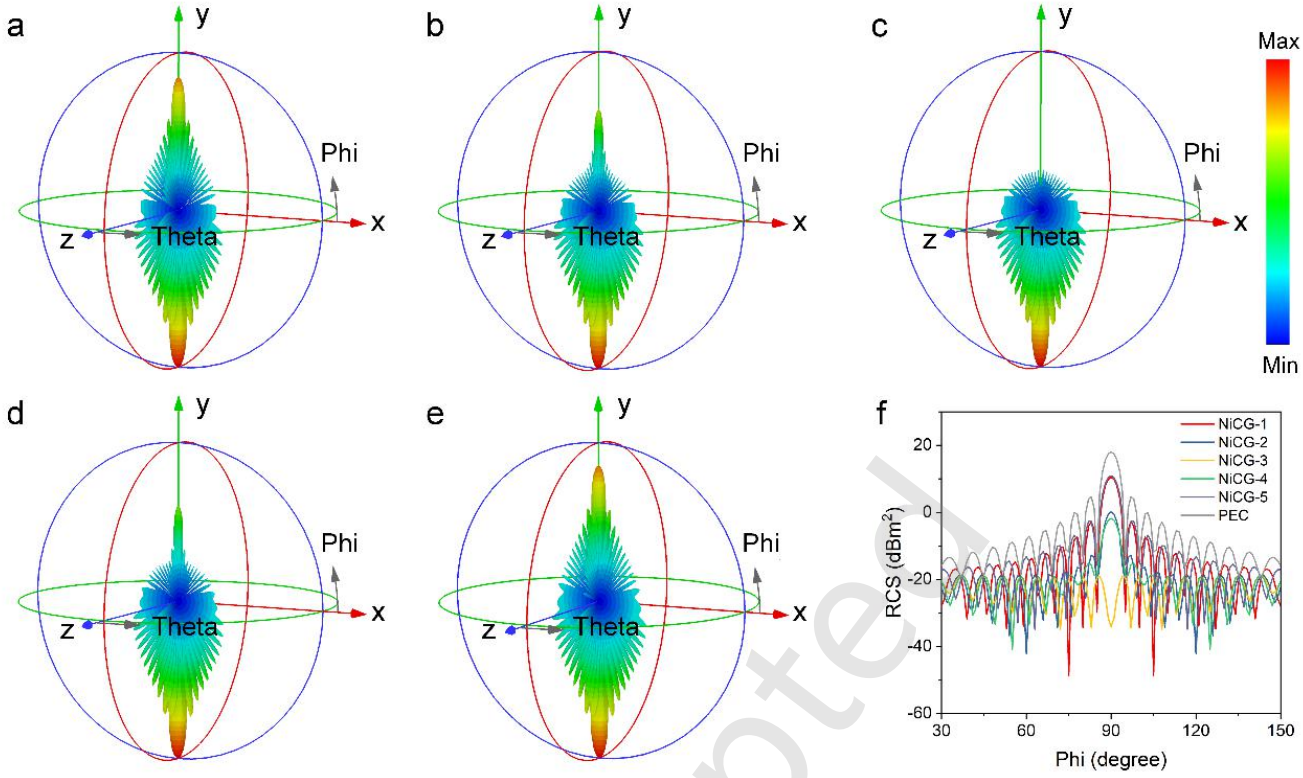

Figure 6 3D radar wave scattering signals of (a) NiCG–1, (b) NiCG–2, (c) NiCG–3, (d) NiCG–4, and (e) NiCG–5 coated on a PEC plate at 16.72 GHz witl a thickness of 2.8 mm. (f) RCS simulation curves of the PEC plate and NiCG–coated models as a function of scanning angle.

below −10 dB is regarded as effective microwave absorption, corresponding to the attenuation of more than 90% of the incident electromagnetic waves. As shown in Fig. 5a–e, the absorption peaks of all samples shift gradually toward lower frequencies with increasing thickness, consistent with the quarter–wavelength cancellation model. NiCG–1 exhibits limited microwave absorption capability, with a minimum RL value of only –10.5 dB at 5.0 mm. With increasing carbonization temperature, the microwave absorption performance is markedly enhanced. NiCG–2 achieves a strong minimum reflection loss (RL_{min}) of –60.0 dB at 4.9 mm and a maximum effective absorption bandwidth (EAB) of 7.0 GHz at 3.3 mm, indicating that a higher carbonization temperature contributes to improved electromagnetic attenuation. Among all samples, NiCG–3 shows the best overall microwave absorption performance, delivering an RL_{min} of –64.0 dB at 2.8 mm and a maximum EAB of 9.0 GHz at 3.4 mm. The 2D RL map of NiCG–3 further visualizes its broad effective absorption region and confirms the coexistence of strong attenuation and broadband absorption (Fig. 5f). The broadened absorption bandwidth and intensified reflection loss can be attributed to the favorable synergy among dielectric loss, magnetic loss, and improved impedance matching [70]. Further increasing the rGO content does not lead to a continuous improvement in microwave absorption performance. NiCG–4 achieves an RL_{min} of –50.2 dB at 3.6 mm and an EAB of 7.5 GHz at 3.2 mm; however, its overall effective absorption bandwidth remains lower than that of NiCG–3. For NiCG–5, although an EAB of 6.4 GHz is achieved at 2.3 mm, the minimum RL value is only –14.3 dB, suggesting a substantially weakened attenuation capability. This performance degradation is mainly associated with the overdeveloped conductive network caused by excessive rGO content. Excessive rGO breaks the balance between complex permittivity and complex permeability, thereby causing impedance mismatch. The EAB – thickness relationship shown in Fig. 5g further confirms the superior broadband absorption capability of NiCG – 3. Compared with the other samples, NiCG – 3 maintains a larger effective absorption bandwidth over a broader thickness range, demonstrating a more favorable balance between attenuation capability and impedance matching. Moreover, comparison with representative aerogel–based microwave absorbers further highlights that NiCG–3 achieves a stronger RL_{min} and a broader EAB at a much lower filling ratio, demonstrating its competitive advantage for lightweight and high–efficiency microwave absorption (Fig. 5h). To further assess the electromagnetic attenuation capability of the NiCG aerogels under simulated far–field conditions, radar cross–section (RCS) simulations were performed [71-74]. A perfect electric conductor (PEC) plate was used as the reference, and the NiCG aerogels were placed on the PEC substrate with a thickness of 2.8 mm at 16.72 GHz. This condition corresponds to the RL_{min} of NiCG–3 and was selected primarily to evaluate its far field scattering behavior under the optimal absorption condition. As shown in Fig. 6a–e, the scattering signals are markedly suppressed for NiCG – 2, NiCG – 3, and NiCG – 4, whereas NiCG–1 and NiCG–5 exhibit relatively limited RCS reduction under this specific simulation condition. For NiCG – 1, the weak suppression mainly arises from its insufficient electromagnetic attenuation capability, which limits the effective dissipation of incident waves within the absorber. In contrast, the limited RCS reduction of NiCG–5 is primarily associated with deteriorated impedance matching caused by an overdeveloped conductive network, leading to enhanced surface reflection and reduced wave penetration. Under the selected simulation condition, NiCG–3 exhibits the weakest backward scattering signal, consistent with its strong microwave absorption at 16.72 GHz and 2.8 mm. The

Under Review Accepted

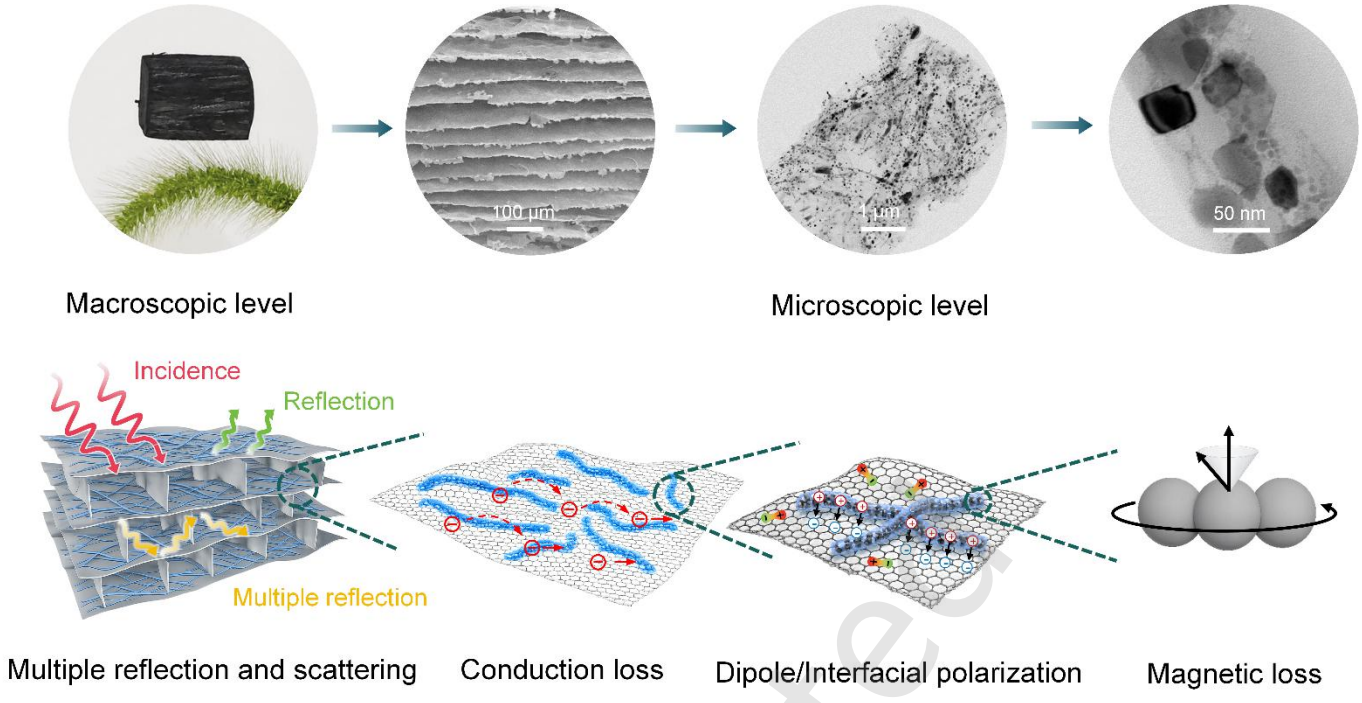

Figure 7 Schematic of the associated microwave absorption mechanism of the proposed Ni–MOF/GO derived magnetic and dielectric aerogels.

corresponding RCS curves in Fig. 6f further corroborate this observation. At 90°, the RCS value of NiCG−3 is reduced by 52.13 dB relative to the PEC plate, indicating pronounced suppression of backward scattering under this condition. This result is consistent with the reflection-loss analysis and indicates the favorable far-field scattering suppression capability of NiCG−3 under its optimal absorption condition.

The superior microwave absorption performance of NiCG−3 can be further understood from the synergistic optimization of impedance matching and electromagnetic attenuation. At the macroscopic level, the anisotropic aerogel framework provides continuous porous channels that facilitate the penetration of incident microwaves and promote repeated reflection and scattering within the internal void space. This process effectively prolongs the propagation pathway of electromagnetic waves and increases their interaction probability with the functional skeleton. At the microscopic level, the rGO framework and Ni – containing magnetic components jointly construct a magnetic – dielectric loss network. The interconnected rGO skeleton provides continuous electron – transport pathways, giving rise to conduction loss under an alternating electromagnetic field. Meanwhile, abundant heterogeneous interfaces between Ni – containing species and rGO, together with defects and residual functional groups in the carbon framework, serve as polarization centers and induce dipolar and interfacial polarization. These polarization relaxation processes contribute to the dissipation of electromagnetic energy as thermal energy. In addition, the Ni – containing magnetic components introduce magnetic loss, including resonance – related dissipation and possible eddy current loss, which further enhances the attenuation of the magnetic – field component of incident microwaves. Therefore, the excellent absorption performance of NiCG−3 originates from the cooperative contribution of its hierarchical porous architecture, conductive rGO network, heterogeneous interfacial polarization, and Ni – containing magnetic loss. These attenuation mechanisms operate cooperatively rather than independently within the lamellar framework, where the porous architecture facilitates wave penetration and propagation, while dielectric and magnetic loss processes subsequently dissipate the electromagnetic energy. The rational balance among these factors enables favorable impedance matching and efficient electromagnetic energy dissipation, thereby accounting for the strong attenuation intensity and broad effective absorption bandwidth of NiCG–3.

4 Conclusion

In summary, ultralight anisotropic magnetic – dielectric graphene aerogels were fabricated by integrating Ni – MOF nanoribbons with GO through ice – templating assembly, freeze–drying, and carbonization. One–dimensional Ni–MOF nanoribbons derived magnetic components were coupled with two – dimensional graphene – derived carbon sheets, creating abundant magnetic – dielectric heterointerfaces throughout the anisotropic porous framework. By tailoring the carbonization temperature and the initial mass ratio of Ni–MOF nanoribbons to GO, the electromagnetic parameters, impedance matching, and attenuation capability of the NiCG aerogels were effectively regulated. The optimized NiCG−3 aerogel exhibited excellent microwave absorption performance, achieving a minimum reflection loss of −64.0 dB at 16.72 GHz under a matching thickness of 2.8 mm and a maximum effective absorption bandwidth of 9.0 GHz at 3.4 mm. Furthermore, comparison with reported aerogel–based absorbers highlights that NiCG−3 achieves strong absorption and broad bandwidth at a relatively low filler content, demonstrating its advantage in lightweight microwave attenuation. These results indicate that Ni – MOF nanoribbons and GO derived magnetic–dielectric graphene aerogels provide a promising platform for lightweight, broadband, and efficient microwave absorption.

Electronic Supplementary Material:

Supplementary material (please give brief details, e.g., further details of the annealing and oxidation

Under Review

procedures, STM measurements, AFM imaging and Raman spectroscopy measurements) is available in the online version of this article at https://doi.org/10.26599/NR.2026.94909330.

Data availability

The data that support the findings of this study are available from the corresponding author upon reasonable request.

Acknowledgements

The authors are grateful to the National Natural Science Foundation of China (52573327, 62071239, 52102361), 333 High-Level Talents Cultivation Project of Jiangsu Province (BRA2022094). Young Elite Scientists Sponsorship Program by Jiangsu Association for Science and Technology (JSTJ2023XH047). China Postdoctoral Science Foundation (2025T180037).

Declaration of competing interest

The authors declare no conflicts of interest.

Author contribution statement

Xiaogu Huang – Supervision; Funding acquisition; Project administration; Formal analysis; Investigation; Methodology; Software; Visualization; Writing – original draft; Gaoyuan Yu – Data curation; Formal analysis; Investigation; Visualization; Writing – original draft; Jiawen Wei – Data curation; Formal analysis; Investigation; Visualization; Gaofeng Shao – Conceptualization; Supervision; Validation; Funding acquisition; Project administration; Writing–review & editing.

Informed consent

Not applicable.

Ethics statement

Not applicable.

Use of AI statement

None.

References

[1] Liu, X.; Zhao, Y.; Zhang, Y.; Cui, X.; Xue, Y.; Lu, X.; Gu, J. Bioinspired Layered-Gradient Nanocomposites for Intelligent Electromagnetic Skins with GHz-THz Wave Absorption, Shielding, and Solvent-Driven Actuation. *Nano-Micro Lett.* **2026**, *18*, 344.

[2] Wang, Z.; Zhao, Z.; Tu, Q.; Yao, C.; Liu, Z.; Zhou, C.; Xu, L.; Guo, S.; Meng, C.; Shao, G.; Cheng, H.; Yang, L. Graphene Aerogel-Based Flexible Pressure Sensor for Physiological Signal Detection and Human-Machine Interaction. *Nano-Micro Lett.* **2026**, *18*, 308.

[3] Ren, B.; Jia, Y.; Qi, L.; Fu, Q.; Lin, Y.; Yu, H.; Cheng, J.; Dai, M.; Song, Q.; Zhang, Y.; Hou, X.; Li, H. Broadband electromagnetic absorption up to 1473 K enabled by dielectric frequency-dispersion engineering in ceramic composites. *Nat Commun.* **2026**, *17*, 318.

[4] Quan, B.; Chen, Y.; Li, L.; Lu, X.; Lou, Z.; Zhu, H.; Zhu, X.; Shao, G.; Guo, T.; Lin, L.; Yu, G.; Huang, X.; Cao, M. Artificially Magnetically Programmed Metamaterial Films for Enhanced Ultra-Wideband Electromagnetic Response. *Adv. Mater.* **2026**, *38*, e20176.

[5] Hou, H.; Yang, Q.; Gao, Y.; Ou, Y.; Wang, Z.; Yi, S.; He, J.; Ma, L.; Meng, F. Progress in supercritical CO_2 foamed polymer composites for electromagnetic protection: from rational structural design to absorption-dominated performance. *Acta Physico-Chimica Sinica*. **2026**, *42*, 100300.

[6] Liao, T.; Li, T.; Zou, Y.; Ma, H.; Yang, Q.; Luo, K.; Han, M.; Meng, F. Bioinspired 4D-Printing Microwave Absorbers With Adaptive Programmable Switches via Morphable Percolation Networks and Resonant Models. *Adv. Mater.* **2026**, *38*, e73633.

[7] Yan, Y.; Lun, A.; Gao, B.; Liu, Y.; Jia, D.; Zhou, Y.; Huang, X. Advances in TMDs-Based Electromagnetic Wave Absorbers: From Structural Engineering to Multicomponent Synergy. *Nano-Micro Lett.* **2026**, *19*, 21.

[8] Li, T. h.; Ma, L.; Wang, L.; Wang, H. b.; Li, B.; Han, M. y.; Li, D. f.; Bai, C. g.; Dong, M. d.; Shen, L. h.; Ma, S.; Qi, F. Ultra-wide band electromagnetic wave absorption by decorating the magnetic particles on two-dimensional $Ti_3C_2T_x$. *Rare Met.* **2025**, *44*, 1844-1855.

[9] Wang, Z. Y.; Li, Z. C.; Li, B.; Shi, A. F.; Zhang, L.; Zhu, Y. B.; Ye, F.; Yu, S. H. Functional Carbon Springs Enabled Dynamic Tunable Microwave Absorption and Thermal Insulation. *Adv. Mater.* **2024**, *36*, 2412605.

[10] Shao, G.; Xu, R.; Chen, Y.; Yu, G.; Wu, X.; Quan, B.; Shen, X.; Huang, X. Miniaturized Hard Carbon Nanofiber Aerogels: From Multiscale Electromagnetic Response Manipulation to Integrated Multifunctional Absorbers. *Adv. Funct. Mater.* **2024**, *34*, 2408252.

[11] Liu, P.; He, Z.; Li, X.; Ding, L.; Liu, S.; Kong, J. Multifunctional Hollow Carbon Microspheres Enable Superior Electromagnetic Wave Response and Corrosion Barrier. *Adv. Mater.* **2025**, *37*, e2500646.

[12] Xiang, H.; Liu, Y.; Su, E.; Su, X.; Xiong, C. Synergistic Optimization of Microwave Absorption and Thermal Properties via Morphology Control in Tin Disulfide Coated FeCoCrNiAl Powders. *Rare Met.* **2026**, *45*, e70313.

[13] Zhou, X. Y.; Zu, C. Z.; Irfan, M.; Dong, K. X.; Yu, W. J.; Wu, M.; Javid, M.; Zhou, Y. L. Construction of hierarchical FeNi@C/ZnO array nanostructures on flexible carbon cloth for high-efficient electromagnetic absorption, self-cleaning, and thermal management. *Rare Met.* **2025**, *44*, 8884-8898.

[14] Li, Y.; Zheng, G.; Yang, K.; Wang, X.; Yang, Y.; Ma, Z. The design of core–shell-structured Fe@Sm2Fe17 dual magnetic nanoparticles for high-performance electromagnetic wave absorption. *Rare Met.* **2025**, *44*, 6503-6512.

[15] Wang, X.; Wang, B.; Zhu, H.; Cao, B.; Liu, T. A Nanoconfinement Strategy to Construct Co@CNTs for Lightweight and Ultra-Broadband Microwave Absorption. *Small.* **2024**, *20*, 2405351.

[16] Cui, R.; Li, Y.; Zhang, X.; Duan, Z.; Zhao, B.; Wan, C. Controlled deintercalation of graphene/organic superlattices with dense atomic-scale steric Schottky heterojunctions for extreme microwave absorption. *Nat Commun.* **2025**, *16*, 5804.

[17] Ding, J.; Shi, R.; Gong, C.; Wang, C.; Guo, Y.; Chen, T.; Zhang, Y.; Cong, H.; Shi, C.; He, F. Defect Engineering Activates Schottky Heterointerfaces of Graphene/$CoSe_2$ Composites with Ultrathin and Lightweight Design Strategies to Boost Electromagnetic Wave Absorption. *Adv. Funct. Mater.* **2023**, *33*, 2305463.

[18] Gao, B.; Yan, Y.; Zhang, K.; Liu, D.; Huang, X. Ultralight Broadband Electromagnetic Wave Absorption Enabled by Interface-Engineered Two-layered Periodic Carbon Fiber Fabrics. *Adv. Funct. Mater.* **2026**, *36*, e32108.

[19] Chen, T.; Yan, Y.; Liu, S.; Cheng, Z.; Gao, B.; Jia, D.; Zhou, Y.; Huang, X. Lightweight and Flexible Fabric Assembled by ANF/GMWCNT Fibers for Broadband Electromagnetic Wave Absorption. *Adv. Funct. Mater.* **2026**, *36*, e28094.

[20] Zhang, T.; Bai, B.; Shao, G.; Du, Y.; Fu, R.; Sai, H. Hierarchically porous aerogels with heterogeneous nanodomains constructed from sub-1 nm nanowires for efficient microwave absorption. *Nano Res.* **2026**, *19*, 94908689.

[21] Zhou, J.; Zhu, Y.; Qian, K.; Miao, M.; Feng, X. Poly(3,4-Ethylenedioxythiophene):Sulfamic Acid Modified Aramid Nanofibers: An Innovative Conductive Polymer With Enhanced Electromagnetic Interference Shielding and Thermoelectric Performance. *Small.* **2024**, *20*, 2405400.

[22] Zhang, L.; Du, J.; Tang, P.; Zhao, X.; Hu, C.; Dong, Y.; Zhang, X.; Liu, N.; Wang, B.; Peng, R.; Zhang, Y.; Wu, G. Regulation of PPy Growth States by Employing Porous Organic Polymers to Obtain Excellent Microwave Absorption Performance. *Small.* **2024**, *20*, 2406001.

[23] Wang, J.; Li, Y.; Cao, J.; Zhang, Y.; Feng, B.; Guo, A.; Yan, L.; Hu, P.; Liu, J. Robust and thermally insulating SiBCN/SiOC ceramic aerogel with superior electromagnetic wave absorption performance and high-temperature stability up to 1600 °C. *J. Adv. Ceram.* **2026**, *15*, 9221256.

[24] Wang, Z.; Wang, S.; Fei, H.; Jiang, T.; Feng, B.; Wen, Q.; Xiong, X. Atomic-scale elucidation of attenuation mechanisms underlying exceptional electromagnetic wave absorption of SiZrBCN ceramic nanocomposites. *J. Adv. Ceram.* **2026**, *15*, 9221221.

[25] Song, L.; Hu, F.; Wang, H.; Wang, L.; Chen, Y.; Wang, H.; Zhang, D.;

Just Accepted

Yuan, X.; Guan, L.; Guo, X.; Yu, K.; Chen, D.; Huang, Y.; Zhang, X.; Bai, Z.; Song, B.; Gao, Q.; Wang, H.; Zhu, Y.; Zhang, R.; Fan, B. Advances in SiC aerogel materials for thermal insulation and electromagnetic wave absorption. *J. Adv. Ceram.* **2026**, *15*, 9221316.

[26] Qi, Q.; Li, T.; Yang, H.; Lv, A.; Liu, Y.; Meng, F. Recent advances in structural engineering of ceramic microwave absorption materials: From nano/micro architectures to macroscale design. *J. Adv. Ceram.* **2025**, *14*, 9221205.

[27] Xia, Y.; Wu, M. X.; Huang, J. T.; Huang, R.; Ding, D. H.; Yin, J.; Xu, C. M.; Yang, H. Y.; Wan, Q. F.; Wang, L. Y.; Liang, B. L.; Lu, Z. C.; Luo, R. Y. Facilitating structural strengthening and electromagnetic wave absorption functionalization of dual-phase SiC ceramics via MBNS-dominated multiphase reinforcement strategy. *J. Adv. Ceram.* **2026**, *15*, 9221234.

[28] He, M.; Hu, J.; Yan, H.; Zhong, X.; Zhang, Y.; Liu, P.; Kong, J.; Gu, J. Shape Anisotropic Chain-Like CoNi/Polydimethylsiloxane Composite Films with Excellent Low-Frequency Microwave Absorption and High Thermal Conductivity. *Adv. Funct. Mater.* **2025**, *35*, 2316691.

[29] Liu, X.; Yu, L.; Zhu, G.; Wang, Z.; Lian, G.; Xiong, X.; You, W.; Che, R. Hollow porous FeCo/Cu/CNTs composite microspheres with excellent microwave absorption performance. *Nano Res.* **2024**, *17*, 9857.

[30] Zuo, X.; Qi, J.; Wen, N.; Sun, C.; Wang, H.; Zhang, Z.; Fan, Z.; Pan, L. Construction of Carbon Foam With Micro-Meso-Macropores and In-Plane Multi-Components for Microwave Absorption. *Adv. Funct. Mater.* **2026**, *36*, e74687.

[31] Zong, J. Y.; Wang, Z. Z.; Cao, W. Q.; Cao, M. S. Flexible and Lightweight Hollow MXene@Carbon Microfiber Composites for Microwave Absorption and Light-Responsive Devices. *Adv. Funct. Mater.* **2026**, *36*, e74876.

[32] Yu, G.; Shao, G.; Xu, Z.; Chen, Y.; Huang, X. Hierarchical interface-engineered magnetic graphene–SiCN aerogels via a stepwise confinement strategy for low-frequency and broadband microwave absorption. *J. Adv. Ceram.* **2025**, *14*, 9221187.

[33] Bian, W.; Liang, X.; Zhao, Q.; Cao, W.; Cao, M. 2D Materials Enabling Intelligent Multispectral Electromagnetic Responses and Devices. *Adv. Mater.* **2026**, *38*, e73095.

[34] Huang, X.; Wei, J.; Zhang, Y.; Qian, B.; Jia, Q.; Liu, J.; Zhao, X.; Shao, G. Ultralight Magnetic and Dielectric Aerogels Achieved by Metal-Organic Framework Initiated Gelation of Graphene Oxide for Enhanced Microwave Absorption. *Nano-Micro Lett.* **2022**, *14*, 107.

[35] Jin, Y.; Cheng, J.; Jiang, S.; Zou, X.; Wang, Y.; Li, Y.; Guo, J.; Ren, Z.; Chen, Q.; Zhang, Z.; Qin, Q.; Liu, B.; Che, R. Conductance Reinforced Relaxation Attenuation with Strong Metal-N Coordination in Multivariate pi-Conjugated MOFs for Integrated Radar-Infrared Camouflage. *Adv. Mater.* **2025**, *37*, 2501330.

[36] Fan, X.-X.; Zhang, X.-C.; Li, L.; Cao, M.-S. Recent progress and perspective of microwave absorption materials derived from metal-organic frameworks. *Soft Science*. **2024**, *4*, 43.

[37] Wu, Q.; Ma, Z.; Wang, C.; Tao, Y.; Wang, S.; Jin, Z.; Gao, T.; Li, C.; Liu, P. Carbon nanofibers with small-sized Co nanoparticles and structural defects via a confined-coordination growth strategy toward electromagnetic wave absorption. *J. Adv. Ceram.* **2025**, *14*, 9221210.

[38] Huang, B.; Ye, F.; Deng, J.; Wang, J.; Li, C.; Cao, Y.; Zhang, W.; Fan, X. Cross-scale structural engineering of MOF-derived CoxNiy@C nanorods with controllable electromagnetic response behavior for broadband electromagnetic wave absorption. *J. Adv. Ceram.* **2026**, *15*, 9221224.

[39] Zhao, R.; Liang, Z.; Zou, R.; Xu, Q. Metal-Organic Frameworks for Batteries. *Joule*. **2018**, *2*, 2235-2259.

[40] Shao, G.; Huang, X.; Shen, X.; Li, C.; Thomas, A. Metal-Organic Framework and Covalent-Organic Framework-Based Aerogels: Synthesis, Functionality, and Applications. *Adv Sci*. **2024**, *11*, e2409290.

[41] Shao, G.; Hanaor, D. A. H.; Shen, X.; Gurlo, A. Freeze Casting: From Low-Dimensional Building Blocks to Aligned Porous Structures-A Review of Novel Materials, Methods, and Applications. *Adv. Mater.* **2020**, *32*, 1907176.

[42] Yu, G.; Shao, G.; Chen, Y.; Xu, Z.; Quan, B.; Zhu, X.; Huang, X. Intelligent Hygroscopic Aerogels: Moisture-Activated Dual-Mode Switchable Electromagnetic Response. *Adv. Funct. Mater.* **2025**, *35*, 2506857.

[43] Wen, C.; Li, X.; Zhang, R.; Xu, C.; You, W.; Liu, Z.; Zhao, B.; Che, R. High-Density Anisotropy Magnetism Enhanced Microwave Absorption Performance in $Ti_3C_2T_x$ MXene@Ni Microspheres. *ACS Nano*. **2022**, *16*, 1150-1159.

[44] Yu, W.; Liu, B.; Zhao, X. Ultralight MOF-Derived Ni_3S_2@N, S-Codoped Graphene Aerogels for High-Performance Microwave Absorption. *Nanomaterials*. **2022**, *12*, 655.

[45] Li, Z.; Deng, L.; Kinloch, I. A.; Young, R. J. Raman spectroscopy of carbon materials and their composites: Graphene, nanotubes and fibres. *Prog. Mater Sci.* **2023**, *135*, 101089.

[46] Huang, X. G.; Yu, G. Y.; Zhang, Y. K.; Zhang, M. J.; Shao, G. F. Design of cellular structure of graphene aerogels for electromagnetic wave absorption. *Chem. Eng. J.* **2021**, *426*, 131894.

[47] Wu, Q.; Li, H.; Wang, J.; Xu, R.; Kim, J.; Li, N.; Cheng, S.; Wang, Y.; Zhao, S.; Nazeeruddin, M. K.; Li, G.; Yang, L. Unveiling Electronic Regulation Mechanism in Amorphous Ni_3S_2/Crystalline Cu Heterointerface for Alkaline Overall Water Splitting. *Adv. Funct. Mater.* **2026**, *36*, e15501

[48] Liang, L.; Li, Q.; Yan, X.; Feng, Y.; Wang, Y.; Zhang, H. B.; Zhou, X.; Liu, C.; Shen, C.; Xie, X. Multifunctional Magnetic $Ti_3C_2T_x$ MXene/Graphene Aerogel with Superior Electromagnetic Wave Absorption Performance. *ACS Nano*. **2021**, *15*, 6622-6632.

[49] Lin, J.; Qiao, J.; Tian, H.; Li, L.; Liu, W.; Wu, L.; Liu, J.; Zeng, Z. Ultralight, hierarchical metal–organic framework derivative/graphene hybrid aerogel for electromagnetic wave absorption. *Adv. Compos. Hybrid Mater.* **2023**, *6*, 177.

[50] Shuang, W.; Huang, H.; Kong, L.; Zhong, M.; Li, A.; Wang, D.; Xu, Y.; Bu, X.-H. Nitrogen-doped carbon shell-confined Ni_3S_2 composite nanosheets derived from Ni-MOF for high performance sodium-ion battery anodes. *Nano Energy*. **2019**, *62*, 154-163.

[51] Zhai, N.; Wang, Z.; Cheng, Z.; Xu, Z.; Guo, K.; Zhou, W.; Gao, F.; Luo, G.; Ji, G. Simultaneous Manipulation of Multidimensional Heterojunctions and Dielectric Gene Engineering for Broadband Microwave Absorption. *Adv. Funct. Mater.* **2025**, *35*, 2502480.

[52] Liang, J.; Ye, F.; Cao, Y.; Mo, R.; Cheng, L.; Song, Q. Defect-Engineered Graphene/Si_3N_4 Multilayer Alternating Core-Shell Nanowire Membrane: A Plainified Hybrid for Broadband Electromagnetic Wave Absorption. *Adv. Funct. Mater.* **2022**, *32*, 2200141.

[53] Yan, Y.; Cheng, Z.; Chen, T.; Zhou, E.; Gao, B.; Qin, G.; Ma, G.; Huang, X. Rational high-entropy doping strategy via modular in situ/post solvothermal doping integration for microwave absorption. *J. Adv. Ceram.* **2025**, *14*, 9221168.

[54] Li, T.; Du, J.; Sun, J.; Liu, Q.; Li, X.; Ou, Y.; Qi, Q.; Liu, Y.; Meng, F. Bioinspired Free-Space Architecture Engineering for Broadband Electromagnetic Absorption and Thermal Management in Graphene-Based Fibrous Textiles. *Adv. Funct. Mater.* **2026**, *36*, e30666.

[55] Yan, Y.; Qin, G.; Zhang, K.; Gao, B.; Ma, G.; Huang, X.; Zhou, Y. Enhancing microwave absorption performance of MoS_2 by synergistic effect of Fe doping. *J. Adv. Ceram.* **2025**, *14*, 9221039.

[56] Qin, M.; Zhang, L.; Wu, H. Dielectric Loss Mechanism in Electromagnetic Wave Absorbing Materials. *Adv Sci*. **2022**, *9*, 2105553.

[57] Liu, C.; Li, J.; Li, S.; Guo, Z.; Chen, Y.; Li, T.; Qin, R.; Sun, J.; Lu, Y.; Meng, F. Neural Network-Based Permittivity Engineering of Magnetic Absorbers for Customizable Microwave Absorption. *Adv Sci*. **2026**, *13*, e21945.

[58] Zeng, X.; Deng, X.; Yu, Z.; Zhang, X.; Lu, J.; Gao, Y. Evolution of Fe Single Atom in SiOC Ceramic Fibers and Their High-Temperature and Ultrathin Electromagnetic Wave Absorption. *Adv. Mater.* **2026**, *38*, e21533.

[59] He, M.; Gu, J. Tunable Low-Frequency Microwave Absorption and Thermal Management through In-Situ Confined Growth of Alloys within Aramid Nanofibers. *Eng. Transform. Mater.* **2026**, *1*, 150.

[60] Sun, R.; Lv, H.; Lian, G.; Wang, L.; Huang, M.; You, W.; Che, R. Dielectric shell regulation in synergy FeCoNi@$ZnIn_2S_4$ microspheres with broadband electromagnetic wave absorption. *Soft Science*. **2025**, *5*, 35.

[61] Niu, R.; Jia, Z.; Lan, D.; Zhang, S.; Gao, Z.; Weng, Z.; Bai, F.; Wu, G. Heterointerface engineering of bimetallic sulfides for augmented polarization loss with electromagnetic wave absorption. *Nano Res.* **2026**, *19*, 94908411.

[62] He, Z.; Xu, H.; Shi, L.; Ren, X.; Kong, J.; Liu, P. Hierarchical Co_2P/CoS_2@C@MoS_2 Composites with Hollow Cavity and Multiple Phases Toward Wideband Electromagnetic Wave Absorption. *Small*. **2024**, *20*, e2306253.

[63] Li, W.; Qi, H.; Guo, F.; Niu, X.; Du, Y.; Chen, Y. $NiFe_2O_4$ nanoparticles supported on cotton-based carbon fibers and their application as a novel broadband microwave absorbent. *RSC Adv*. **2019**, *9*, 29959-29966.

[64] Zhang, M.; Jiang, Z.; Lv, X.; Zhang, X.; Zhang, Y.; Zhang, J.; Zhang, L.; Gong, C. Microwave absorption performance of reduced graphene oxide with negative imaginary permeability. *J. Phys. D: Appl. Phys.*

Just Accepted

2019, *53*, 02lt01.
[65] Liu, X.; Qian, Y.; Yu, L.; Si, Z.; Wu, L.; Wan, G.; Xu, X.; Wang, G. Regulating Local Coordination Environment of Single-Atom Co Absorbers for Dielectric-Magnetic Dual Loss Modulation. *Adv. Mater.* **2026**, *38*, e72966.
[66] Cui, Z.; Li, X.; Zhang, H.; Han, G.; Fang, M.; Wang, Y.; Fang, X.; Yan, L.; Yan, Q.; Yu, R.; Shui, J.; Liu, X. Tailoring sulfur/nitrogen co-doping configuration in MXene nanoribbon/nanosheet composite for high-performance electromagnetic wave absorption. *J. Adv. Ceram.* **2025**, *14*, 9221209.
[67] Qi, J.; Liang, C.; Ruan, K.; Li, M.; Guo, H.; He, M.; Qiu, H.; Guo, Y.; Gu, J. Cactus-like architecture for synergistic microwave absorption and thermal management. *Natl Sci Rev*. **2025**, *12*, nwaf394.
[68] Ding, L.; He, Z.; Zhang, R.; Liu, S.; Geng, W.; Liu, P. Hollow $Zn_{1-x}Co_{2-y}Ni_xFe_yO_4$ spinel via multi-metal ion doping: ultralight and broadband microwave absorber. *Soft Science*. **2026**, *6*, 2.
[69] Shi, H.; Gao, H.; Qin, L.; Yuan, J. T.; Tang, L. X.; Wang, Z. R.; Li, W. J.; Feng, Z. H.; Wang, Y.; Xie, A. M. High efficiency electromagnetic waves absorption of ferrite/polypyrrole composite based on precise structural control of rare earth doping. *Rare Met.* **2025**, *44*, 5621-5632.
[70] Wu, Z.; Huang, J.; Zeng, X. Dual magnetic particles modified carbon nanosheets in CoFe/Co@NC heterostructure for efficient electromagnetic synergy. *Soft Science*. **2024**, *4*, 42.
[71] Chen, Y.; Chen, M.; Lei, H.; Song, L.; Zhang, R.; Li, H.; Tian, M.; Fan, B. Microwave-assisted synthesis of high-performance TaC nanorods for enhanced electromagnetic wave absorption. *J. Adv. Ceram.* **2025**, *14*, 9221130.
[72] Wen, L.; Cheng, S.; Shang, H.; Sheng, D.; Li, W.; Qi, X.; Xie, A. Regulating Interfacial Strain from Tensile to Compressive State in Transition-Metal-Sulfides/Carbon for High-Performance Electromagnetic Wave Absorption. *Adv. Funct. Mater.* **2026**, *36*, e74621.
[73] Zhang, G.; Zhang, R.; Zeng, Z.; Liu, B.; Hou, Y.; Zhong, B.; Xia, L.; Wen, G.; Wang, D.; Huang, X. Electron Delocalization Engineering on 2D High-Entropy Metal Oxides for Boosting Electromagnetic Wave Absorption. *Adv. Funct. Mater.* **2026**, *36*, e27135.
[74] Yang, Q.; Hou, H.; Lu, Y.; Guo, Z.; Sun, J.; Zhang, P.; Yang, T.; Meng, F. Cascaded Broadband Low-Frequency Microwave Absorption Covering P- to C-Band in Ultra-Thin Metamaterials via Synergistic Local‐Field and Loss‐Field Enhancement. *Nano-Micro Lett.* **2026**, *18*, 407.

Just Accepted

Electronic Supplementary Material

Ice-templated lamellar aerogels with magnetic-dielectric synergy derived from Ni-MOF nanoribbons/graphene for ultralight broadband microwave absorption

Xiaogu Huang [1] ✉, Gaoyuan Yu [1], Jiawen Wei [1], Gaofeng Shao [1] ✉

[1] School of Chemistry and Materials Science, Jiangsu Key Laboratory of New Energy Devices and Interface Science, Nanjing University of Information Science & Technology, Nanjing 210044, China

Supporting information to https://doi.org/10.26599/NR.2026.94909330

Just Accepted

Address correspondence to Xiaogu Huang, hxg@nuist.edu.cn; Gaofeng Shao, gfshao@nuist.edu.cn



Fig. S1 Digital photograph of the NiCG–3 aerogel.

Just Accepted

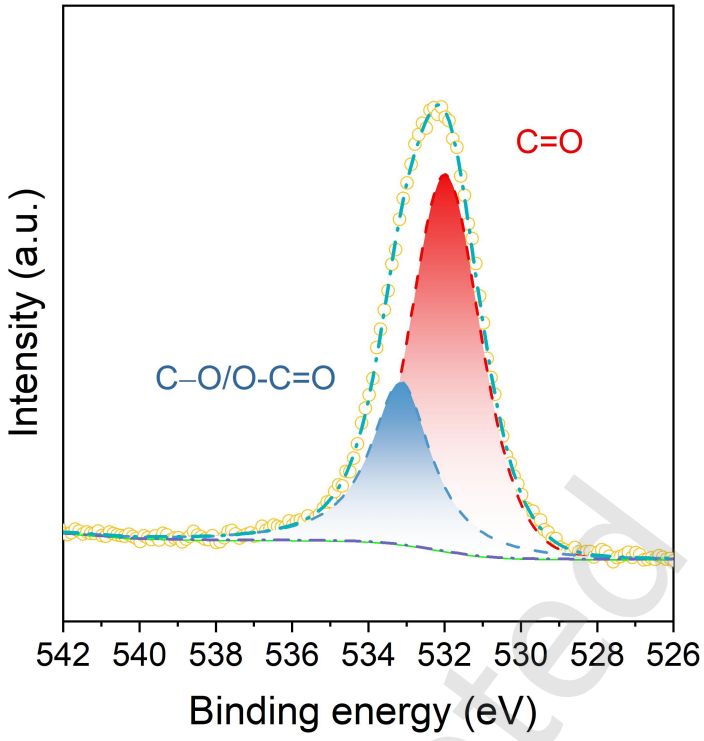

Fig. S2 High–resolution XPS spectra of O 1s for the NiCG–3 aerogel.

Just Accepted

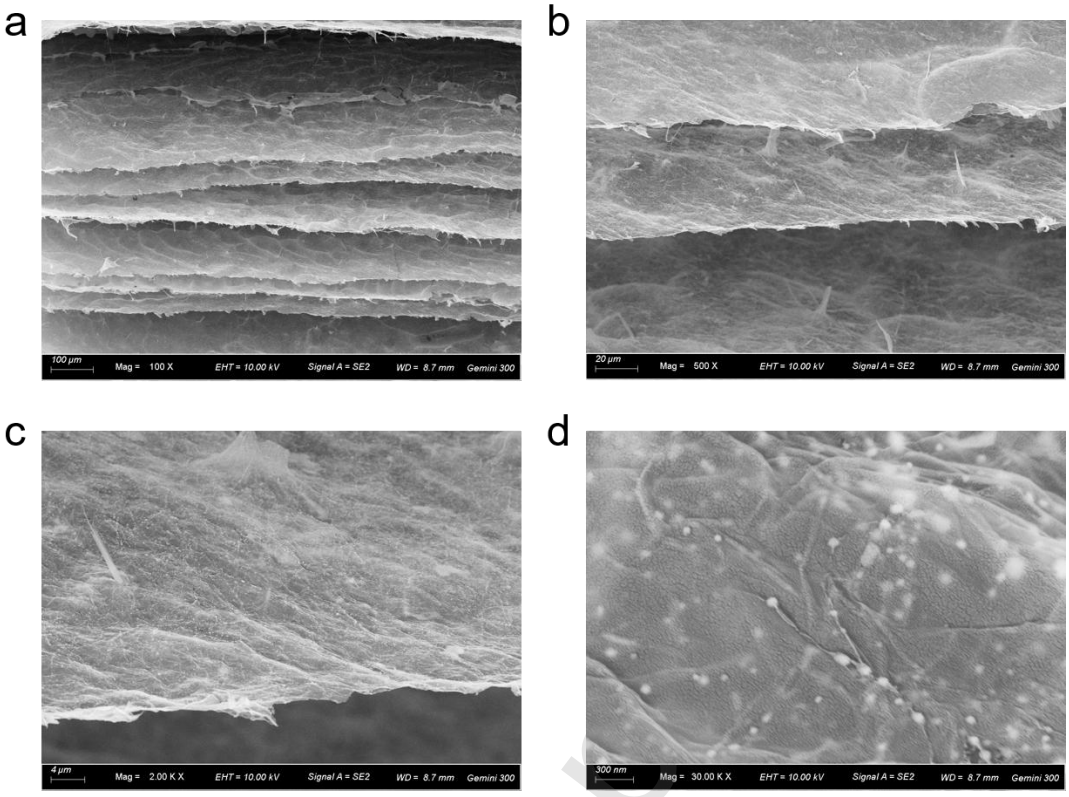

Fig. S3 SEM images of the NiCG–4 aerogel.

Just Accepted

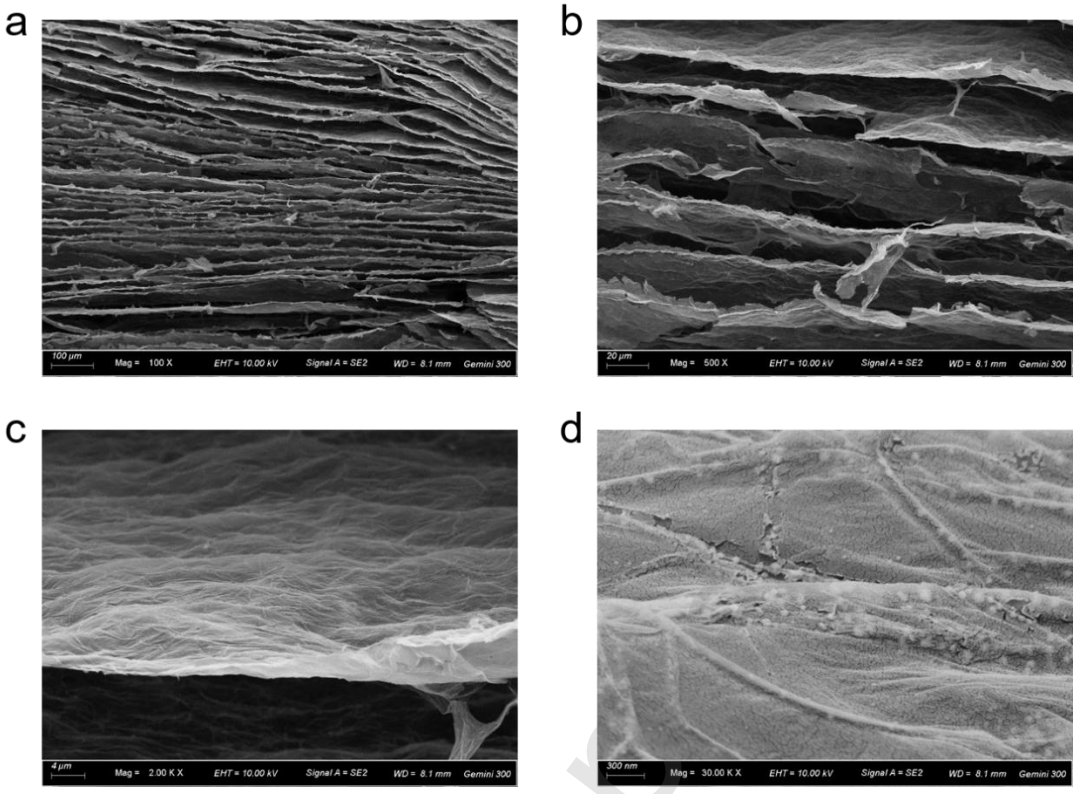

Fig. S4 SEM images of the NiCG–5 aerogel.

Just Accep

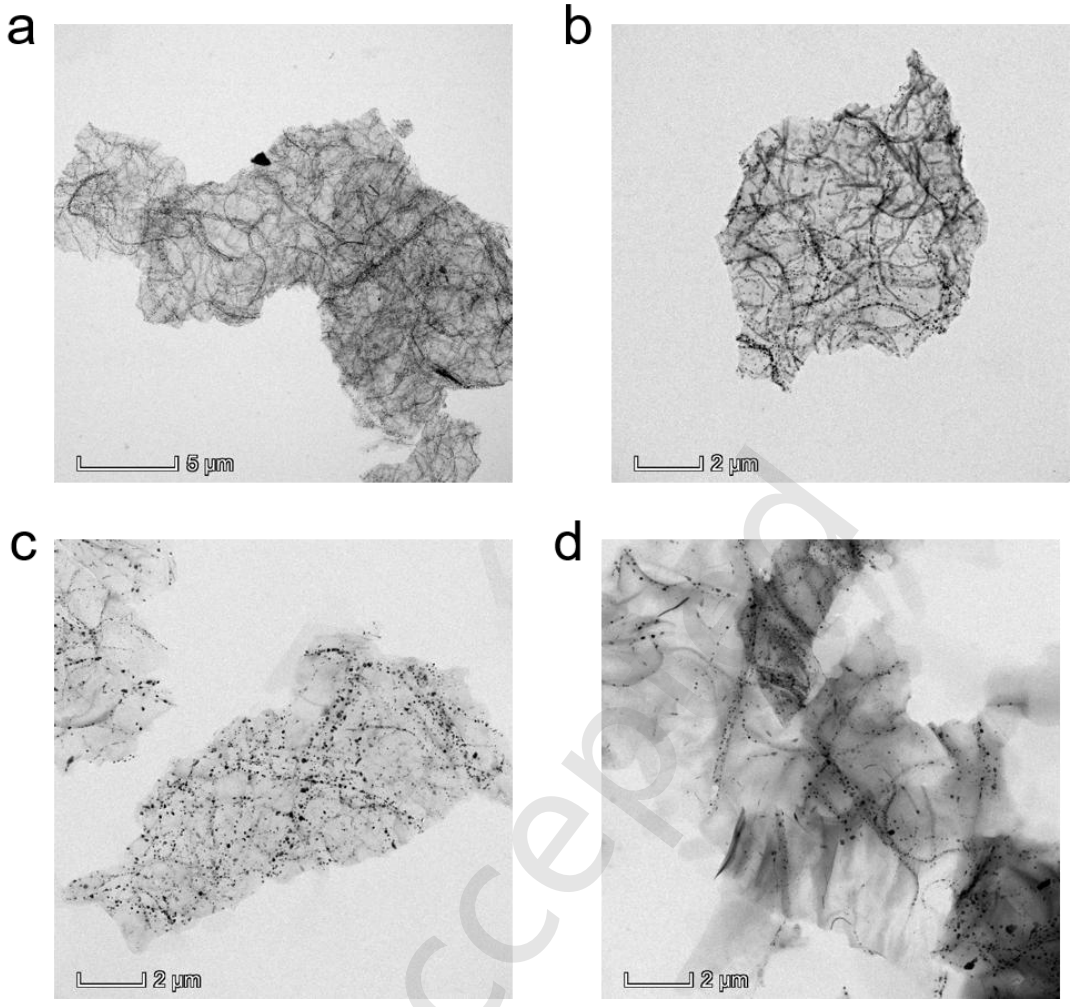

Fig. S5 TEM images of (a) NiCG–1, (b) NiCG–2, (c) NiCG–4, (d) NiCG–5.

Just Accepted

Table S1. The electromagnetic wave absorbing performance comparison of reported aerogel–based absorbers in recent years.

Materials	Fill content (%)	RL (dB)	EAB (GHz)	Refs.
NFNCA	20	−53.49	6.24	[1]
FCM	50	−49.94	5.44	[2]
SCA	10	−44.89	5.8	[3]
SPCA@Co	30	−52.50	4.52	[4]
$Fe_3C@CeO_2/NC$	3	−64.63	5.3	[5]
CNMX	7	−48.5	5.2	[6]
$1T–WS_2/CNT\text{-}rGO$	30	−56.63	3.84	[7]
C@NCO	50	−54.6	5.7	[8]
LPA	10	−63.98	8.85	[9]
CNA@FeCoNi	5	−56.7	5.28	[10]
PI~NC-GAMs	1	−63.6	7.45	[11]
NiCG	0.5	−64	9	This work

Just Accepted

References

[1] Du X, Zhou J, Yu J, Nie X, Luo M, He X, Xiao A. Self-Sensing NiFe@N-doped Carbon Aerogel: Integrating Excellent Radar Stealth, Inherent Structural Health Monitoring, Thermal Management, and Flame Retardancy. Nano-Micro Lett. 2026; 18: 278. https://doi.org/10.1007/s40820-026-02128-5.

[2] Li C, Liang L, Zhang B, Yang Y, Ji G. Synergistic customization of interfacial engineering MXene-integrated aerogels enable multifunctional radar-infrared stealth. Chem Eng J. 2025; 520: 166211. https://doi.org/10.1016/j.cej.2025.166211.

[3] Han X, Feng Y, Zhang N, Du W, Zhang W, Yu Q, Liu Y, Wang B, Jiang F, Liu L, Xu L, Zhang X. Bio-based multifunctional carbon aerogels for ultrawide electromagnetic wave absorption and thermal insulation. Carbon. 2025; 238: 120231. https://doi.org/10.1016/j.carbon.2025.120231.

[4] liu Z, Wang L, Zhao Y, Ren J, Wang H, Hu J, Guan H. Environmental adaptability and efficient electromagnetic wave protection of C/Co aerogels by anchoring Co to biomass carbon via the high-temperature induced morphological transformation of ZIF-67. Nano Res. 2025; 18: 94907581. https://doi.org/10.26599/nr.2025.94907581.

[5] Zhao PY, Peng HL, Cai B, Zhou L, Liang CM, Koo MC, Wang HY, Wu J, Hou ZL, Wang GS. Mechanism Decoupling of Impedance Matching and Attenuation Enhancement via Spatial Distribution of Loading Components. Adv Funct Mater. 2025; 36: e18479 https://doi.org/10.1002/adfm.202518479.

[6] Zhao H, Zhang C, Li Y, Sun J, Yang X, Yu L, Zhou E, Liu D, Ren Z, Sun X, Yang L, Cheng Y, Wang C, He J, Lv H. Ordered cellular 2D/2D biomass-derived carbon nanosheet/MXene aerogels for ultralight and high-performance microwave absorption. J Adv Ceram. 2025; 14: 9221214. https://doi.org/10.26599/jac.2025.9221214.

[7] Zhou J, Luo J, Hao G, Guo F, Liu G, Guo H, Zhang G, Xiao L, Hu Y, Jiang W. A freestanding 3D heterophase tungsten disulfide-based aerogel as an ultrathin microwave absorber in the Ku-band. Journal of Materials Chemistry A. 2022; 10: 13848-13857. https://doi.org/10.1039/d2ta02520e.

[8] Kang S, Qiao S, Cao Y, Hu Z, Yu J, Wang Y. Compression strain-dependent tubular carbon nanofibers/graphene aerogel absorber with ultrabroad absorption band. Chem Eng J. 2022; 433: 133619. https://doi.org/10.1016/j.cej.2021.133619.

[9] Wang S, Cheng Z, Yan Y, Yao J, Liu Y, Tao J, Duan L, Weng Y, Zhu H, Zhuang H, Zhou J, Hao X. Programmable Electromagnetic Switching in Shape-Memory-Driven Liquid Metal/Polyimide/Aramid Nanofiber Aerogels for Intelligent Wave Management. Adv Funct Mater. 2025; 36: e21612 https://doi.org/10.1002/adfm.202521612.

[10] Nie W, Wang B, Wu W, Li S, Huang F, Ma W, Zhang H. In Situ Growth Medium Entropy Alloy Nanoparticles on the Ordered Structure Carbon Nanofiber Aerogel for Enhanced Microwave Absorption and Infrared Stealth Properties. Small. 2025; 21: 2503955. https://doi.org/10.1002/smll.202503955.

[11] Cai Y, Wang Z, Fei G, Lavorgna M, Xia H. Polyimide Derived Carbon/Graphene Hybrid Aerogel Microspheres for Strong and Wide Bandwidth Microwave Absorption. Adv Funct Mater. 2025; 35: 2419252. https://doi.org/10.1002/adfm.202419252.

Just Accepted